Comet P/2010 TO20 LINEAR-Grauer as a Mini-29P/SW1

Lacerda, P. (2013). Comet P/2010 TO20 LINEAR-Grauer as a Mini-29P/SW1. *Monthly Notices of the Royal Astronomical Society*, *428*(2), 1818-1826. https://doi.org/10.1093/mnras/sts164

Published in:
Monthly Notices of the Royal Astronomical Society

Document Version:
Publisher's PDF, also known as Version of record

Queen's University Belfast - Research Portal:
Link to publication record in Queen's University Belfast Research Portal

Monthly Notices
of the
ROYAL ASTRONOMICAL SOCIETY

MNRAS **428,** 1818–1826 (2013) doi:10.1093/mnras/sts164

Comet P/2010 TO20 LINEAR-Grauer as a Mini-29P/SW1

Pedro Lacerda★†

Astrophysics Research Centre, School of Mathematics and Physics, Queen's University Belfast, Belfast BT7 1NN

Accepted 2012 October 4. Received 2012 October 4; in original form 2012 July 24

ABSTRACT

Discovered in 2010 October by the Lincoln Near-Earth Asteroid Research (LINEAR) survey, P/2010 TO20 LINEAR-Grauer (P/LG) was initially classified as an inert Jupiter Trojan. Subsequent observations obtained in 2011 October revealed P/LG to be a Jupiter-family comet (JFC). P/LG has one of the largest perihelia ($q = 5.1$ au) and lowest eccentricities ($e = 0.09$) of the known JFCs. We report on observations of P/LG taken on 2011 October 29 and numerical simulations of its orbital evolution. Analysis of our data reveals that P/LG has a small nucleus (<3 km in radius) with broad-band colours ($B - R = 0.99 \pm 0.06$ mag, $V - R = 0.47 \pm 0.06$ mag) typical of JFCs. We find a model-dependent mass-loss rate close to 100 kg s^{-1}, most likely powered by water–ice sublimation. Our numerical simulation indicates that the orbit of P/LG is unstable on very short (10–100 yr) time-scales and suggest that this object has recently evolved into its current location from a more distant, Centaur-type orbit. The orbit, dynamics and activity of P/LG share similarities with the well-known case of comet 29P/Schwassmann–Wachmann 1.

Key words: methods: data analysis – techniques: photometric – comets: individual: P/2010 TO20 LINEAR-Grauer – minor planets, asteroids: general.

1 INTRODUCTION

Jupiter-family comets (JFCs) originate in the trans-Neptunian region of the Solar system known as the Kuiper belt. Kuiper belt objects (KBOs) preserve key information about the epoch of planetesimal formation. The low ambient temperature (∼40 K) allows KBOs to retain most if not all of the ices present in their formation environment. This makes them valuable time capsules with which to study an epoch long gone. JFCs represent the small end of the steep size distribution of KBOs. They are survivors of a dynamically intermediate population, the Centaurs, that were neither ejected from the Solar system nor collided with one of the giant planets (Jupiter to Neptune) on their journey from the Kuiper belt into the inner Solar system.

The surfaces of JFCs are heavily processed when compared to KBOs, mainly by sublimation of surface ice. Indeed, the optical broad-band colours of the two populations differ substantially: JFCs have typically solar (neutral) colours ($B - R \sim 1.3$, $g - r \sim 0.6$), with a spread of about 0.2 mag (Lamy & Toth 2009; Solontoi et al. 2012) while KBOs span a broad range of optical colours, from neutral ($B - R \sim 1$) to very red ($B - R \sim 2.5$; Jewitt & Luu 2001; Jewitt 2002). The neutral surfaces are usually attributed to a fresh ice coating while very red surfaces are thought to be the end product of irradiation of initially neutral material (Thompson et al. 1987; Moroz et al. 1998). The intermediate Centaurs present a peculiar, also intermediate distribution of colours which includes neutral objects (blue group) and very red objects (red group) but very few cases in between (Peixinho et al. 2003). This Centaur colour bimodality may be related to their dynamical history (Melita & Licandro 2012) or simply to the fact that they are small (Peixinho et al. 2012).

Some objects straddle the line between Centaurs and JFCs. They are active, like JFCs, but have Centaur-like orbits. A famous example is 29P/Schwassmann–Wachmann 1 (hereafter 29P). The orbit of 29P is nearly circular ($e = 0.04$) with perihelion and semimajor axis beyond Jupiter ($q = 5.7$ au and $a = 6.0$ au) and obeys the dynamical definition of a Centaur. 29P is constantly active and displays sporadic photometric outbursts (Roemer 1958; Jewitt 1990; Trigo-Rodríguez et al. 2008). The activity of 29P is mainly driven by carbon monoxide sublimation (Senay & Jewitt 1994; Crovisier et al. 1995). Comet 29P has a radius $r = 23 \pm 3$ km (Yan Fernández, private communication).

In this paper, we present a study of comet P/2010 TO20 LINEAR-Grauer (hereafter P/LG) which is in many respects similar to 29P. Comet P/LG has a low eccentricity ($e = 0.09$), high perihelion ($q = 5.1$ au) orbit, very close to meeting the Centaur definition (see Table 1 and Fig. 1). When P/LG was discovered by the Lincoln Near-Earth Asteroid Research (LINEAR) survey, on 2010 October 1, it was misclassified as a Trojan and its weak activity went unnoticed. We present optical broad-band measurements of P/LG and numerical simulations of its orbital evolution. The former show that

★ E-mail: lacerda.pedro@gmail.com

†Some of the presented data were obtained at the European Southern Observatory (ESO) facilities at La Silla under programme 088.C-0634A.

Table 1. Orbital properties of LINEAR-Grauer on 2011 October 29.

Property	Value
Semimajor axis, a	5.610 au
Eccentricity, e	0.087
Inclination, i	2.°628
Argument of perihelion, ω	252.°9
Longitude of ascending node, Ω	44.°03
Mean anomaly, M	84.°22
True anomaly, ν	94.°19
Last perihelion passage	2008 Sep 5
Perihelion distance, q	5.122 au
Aphelion distance, Q	6.097 au

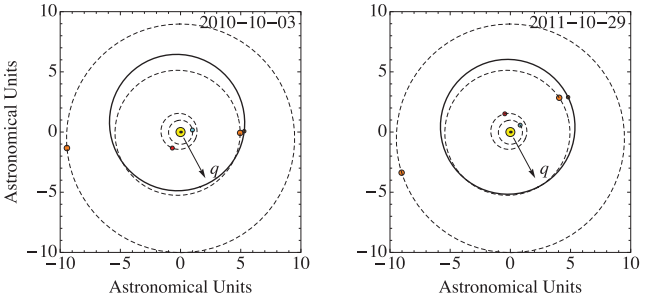

Figure 1. Osculating orbit of P/LG on 2010 October 3 (near the time it was discovered by LINEAR) and on 2011 October 29, when the observations reported here were taken. Due to the proximity to Jupiter the osculating orbit of P/LG changed significantly in a period of only 1 yr. An arrow marks the direction to the last perihelion, the orbits of Earth, Mars, Jupiter and Saturn are plotted as dashed lines and the axes are labelled in astronomical units.

P/LG is weakly active, at a level comparable to the active Centaurs (Jewitt 2009) while the latter indicate that P/LG has in all likelihood recently evolved into its current location from a Centaur orbit. The implication is that P/LG may offer a glimpse of a relatively small and fresh Centaur object.

2 OBSERVATIONS

P/LG was observed on 2011 October 29 at the ESO New Technology Telescope (NTT) located at the La Silla Observatory, Chile. The night was photometric and the seeing varied between 0.8 and 1.0 arcsec. At the NTT we used the EFOSC2 instrument (Buzzoni et al. 1984; Snodgrass et al. 2008) which is installed at the *f*/11 Nasmyth focus and is equipped with a LORAL 2048 × 2048 CCD. We used the 2 × 2 binning mode to bring the effective pixel scale to 0.24 arcsec pixel^{-1}. Our observations were taken through Bessel *B*, *V*, *R* filters (ESO 639, 641, 642, respectively).

The images of P/LG were collected in a relatively regular fashion, in sets of three consecutive exposures per filter, with exposure times of 240 s for *B* and 120 s for *V* and *R*. In total, we collected 12 images in the *B* band, 12 in the *V* band and 18 in the *R* band. Throughout the observations of P/LG, the telescope was set to track the non-sidereal motion of P/LG at an approximate rate of −18 arcsec h^{-1} in right ascension and −6 arcsec h^{-1} in declination.

Bias calibration frames and dithered twilight flats through all three filters were collected on the same night as the science data. The reduction of the science images, consisting of standard bias subtraction and flat fielding, was done using the IRAF `ccdproc` routines. The *R*-band images suffered from fringing which was removed using an IRAF package optimized for EFOSC2 that was kindly supplied by Colin Snodgrass. The P/LG data were absolutely calibrated using observations of Landolt (1992) stars taken throughout the night.

P/LG was observed as part of the Pan-STARRS PS1 all-sky survey very near the time of its discovery by LINEAR. Located on Haleakala, Maui, the 1.8-m PS1 telescope is equipped with a 1.4 gigapixel camera covering 3.°2 × 3.°2 on the sky. The survey repeatedly covers the 3π steradians of sky visible from Haleakala. PS1 uses a photometric system that approaches the Sloan Digital Sky Survey filter system with the addition of a wide (w) band filter which roughly corresponds to the combined passband of the *gri* filters (Tonry et al. 2012). The PS1 gigapixel camera has a pixel scale of 0.25 arcsec pixel^{-1}. P/LG was imaged in four consecutive 45-s exposures taken through the w filter on 2010 October 3. All images were processed automatically by the Pan-STARRS Image Processing Pipeline.

3 COMET MORPHOLOGY

Fig. 2 shows *R*- and *B*-band summed stacks of P/LG and Fig. 3 shows enlarged sections of the region surrounding the nucleus of P/LG, to highlight details. A description of how the stacks were assembled can be found in Sections 4.1 and 4.3; here we focus solely on inspecting the overall appearance of the comet. The projected comet tail is clearly visible and extends for more than 1 arcmin in the direction opposite the orbital motion. Due to the very small solar phase angle, the antisolar direction points almost radially away from the observer. As a result, the projected, antisolar component of the cometary tail is tiny, and more easily viewed in the enlarged, median-filtered version shown in Fig. 3. The bulk of the tail particles trails the comet as a result of Keplerian shear. The Laplacian-filtered image (Fig. 3) displays a darker ridge at the centre of the tail which originates in the nucleus and is aligned with the orbital motion. The ridge is probably due to large particles leaving the nucleus. Larger particles attain lower ejection velocities as they couple more weakly to the sublimating gas and hence tend to remain concentrated in the plane of the orbit where solar radiation acts to push them radially outwards and Keplerian shear forces them to trail the nucleus.

Fig. 4 shows a stack of four consecutive w-band images of comet P/LG taken by the PS1 survey. The PS1 images are taken only 2 d after discovery by LINEAR on 2010 October 1. The comet appears active, with a tail that extends about 12 arcsec on the sky. Here, as in the case of our more recent observations, the solar phase angle is small, just over 2°, probably causing the tail to extend mainly into the plane of the sky along the line of sight. As above, the near-nucleus portion of the sky-projected tail seems to be antisolar, but further from the nucleus the tail seems to trail the nucleus along the orbital direction. The three sets of images show that P/LG was active at the time of discovery (2010 October) and remains active a year later (2011 October).

4 PHOTOMETRY

We performed aperture photometry of comet P/LG and nearby field stars using the IRAF `apphot` task with four main goals: (1) to estimate the size of the comet nucleus, (2) to estimate the mass-loss rate from the comet, (3) to measure the colour of the nucleus and coma dust and (4) to search for brightness variations in the nucleus and coma over time. With those goals in mind, we extracted photometric data from the science images using four synthetic apertures defining four regions of interest (see Table 3). The central region, $\mathcal{R}_4$, 4 pixel (0.96 arcsec) in radius, was selected to represent the flux from the nucleus, but includes an unknown fraction of light due to

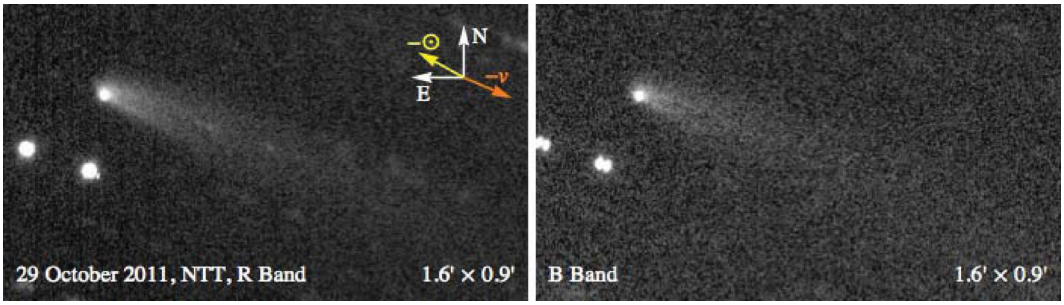

Figure 2. Summed stacks of nine *R*-band (left) and six *B*-band (right) images of comet P/LG. The projected tail is more than 1 arcmin long and points in the direction opposite the orbital motion ($-v$). Because of the very small solar phase angle (Table 2), the antisolar direction lies nearly perpendicular to the plane of the sky. For this reason, the near-nucleus tail has only a small component in the projected antisolar direction ($-\odot$; see Fig. 3) which rapidly bends towards the direction opposite the orbital motion.

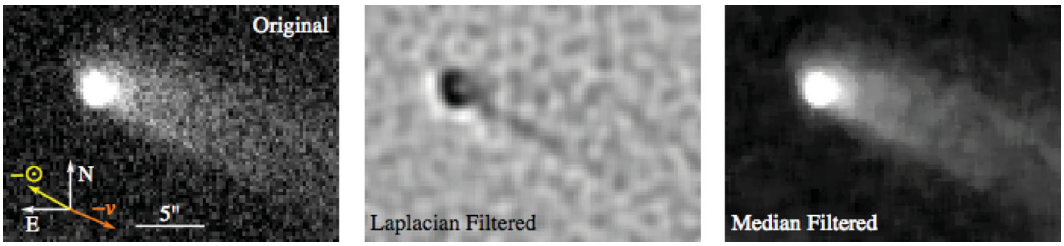

Figure 3. Enlarged versions of the near-nucleus tail structure from the *R*-band stack shown in Fig. 2. The original image (left) is shown together with versions processed using Laplacian (centre) and median (right) filters. A trail of larger particles leaving the nucleus and trailing the comet's orbital motion is visible in the Laplacian-filtered image. The median-filtered image highlights the near-nucleus part of the tail which points in the projected antisolar direction.

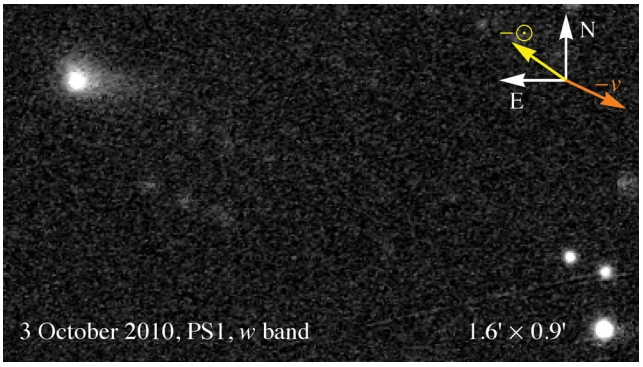

Figure 4. Stack of four consecutive Pan-STARRS w-band images of P/LG taken on 2010 October 3, very near the time of its discovery by the LINEAR survey. The comet is clearly active in these images.

the coma. The intermediate annulus, $\mathcal{R}_{4,8}$, between 4 and 8 pixel (0.96 and 1.92 arcsec) from the nucleus includes contributions from both the nucleus point spread function (PSF) and the coma. The annular region $\mathcal{R}_{8,13}$, located between 8 and 13 pixel (1.92 and 3.12 arcsec) from the nucleus, is dominated by the coma. Finally, the outer annulus $\mathcal{R}_{13,20}$, located between 13 and 20 pixel from the nucleus (3.12 and 4.8 arcsec), includes coma flux and significant noise contamination. Details of how these particular apertures were chosen can be found in Sections 4.1, 4.2 and 4.3. Magnitudes measured in these regions are labelled m_4, $m_{4,8}$, $m_{8,13}$ and $m_{13,20}$. Magnitudes within the annuli, labelled $m_{\rm in,\,out}$, were calculated from the magnitudes within the inner and outer apertures, $m_{\rm in}$ and $m_{\rm out}$, through

$$m_{\rm in,out} = -2.5\log_{10}\left(10^{-0.4m_{\rm out}} - 10^{-0.4m_{\rm in}}\right).$$

We list the *B*, *V* and *R* apparent magnitudes in each region in Table 4.

4.1 Nucleus size

To estimate the radius of the nucleus of comet P/LG, we began by generating a summed stack of nine *R*-band frames that were shifted and aligned at the comet nucleus position. The stack, displayed in Fig. 2, has an equivalent integration time of 1080 s and offers an enhanced signal-to-noise ratio (S/N) detection of the comet. We used the *R*-band images because they are sharper (better seeing) and have higher S/N than those in *B* and *V*. The particular frames that were stacked have seeing between 0.8 and 0.9 arcsec. An analogous stack that aligns the field stars instead of the comet was used to investigate the best choice of aperture for the photometry. We found that a 4-pixel radius aperture, containing ∼85 per cent of the flux of a point source, offers the best compromise between maximizing the S/N within the aperture and minimizing the contribution from surrounding sources. We labelled this region $\mathcal{R}_4$ and used the magnitude within it, m_4, as best representing the flux from the nucleus. In the case of comet P/LG we obtain an $\mathrm{S/N}_R \sim 75$ within the central region $\mathcal{R}_4$ and measure an *R*-band magnitude $m_4 = 20.95 \pm 0.03$ mag.

Assuming a spherical cometary nucleus with cross-section $\pi r_{\rm e}^2$, we calculated the equivalent radius $r_{\rm e}$ using the relation (Russell 1916)

$$\pi r_{\rm e}^2\, p_R \times 10^{-0.4\beta\alpha} = 2.25\times10^{22}\,\pi\,R^2\,\Delta^2 \times 10^{-0.4(m_4 - m_\odot)}, \quad (1)$$

where p_R is the *R*-band geometric albedo and β is the linear phase coefficient of the nucleus. Table 2 lists the values of the solar phase angle, α, heliocentric distance, R, and geocentric distance, Δ, of P/LG on 2011 October 29. The apparent red magnitude of the Sun at Earth is $m_\odot = -27.1$ mag. The values of p_R and β are unknown for P/LG. The uncertainty introduced by β is negligible when compared to that in p_R (uncertain by a factor of 2 or more) because P/LG was observed at very low phase angle ($\alpha < 1^\circ$). We used $\beta = 0.02$ mag deg^{-1} (Millis, Ahearn & Thompson 1982;

Table 2. Observing geometry.

Property	2010 October 3	2011 October 29
Solar phase angle, α (°)	2.07	0.89
Heliocentric distance, R (au)	5.295	5.603
Geocentric distance, Δ (au)	4.309	4.613
1 arcsec at distance Δ (km)	3135	3355

Meech & Jewitt 1987) and $p_R = 0.1$ (Kolokolova et al. 2004) and found an equivalent radius $r_e < 3$ km. This figure is an upper limit due to the unknown contribution of dust coma to the flux within the central aperture.

The apparent magnitude of P/LG may be converted to a nucleus absolute magnitude, $m(1, 1, 0)$ (the theoretical magnitude of the nucleus when placed at 1 au from the Sun and the Earth, and seen at 0° phase angle), using

$$m(1, 1, 0) = m_4 - 5\log_{10}(R\Delta) - \beta\alpha. \quad (2)$$

Substituting the quantities R, Δ and α from Table 2 and again using $\beta = 0.02$ mag deg^{-1} we obtain $m_R(1, 1, 0) = 13.04 \pm 0.03$ mag. The formal error in $m(1, 1, 0)$ is the same as that in the apparent red magnitude, but the true uncertainty is higher due to the unknown value of β. We also note that this is a lower limit to the absolute magnitude of the P/LG nucleus because of the unknown contribution of near-nucleus coma to the magnitude m_4.

4.2 Mass-loss rate

An order of magnitude estimate of the mass-loss rate from P/LG can be calculated by dividing the total dust mass present within a coma-dominated annulus surrounding the nucleus by the time it takes the dust to cross the annulus (Jewitt & Luu 1989). As given in Section 4.1 we used the nine-frame, R-band stack to measure the amount of sunlight-reflecting dust within the annular region. The annulus was set between 8 and 13 pixel from the nucleus photocentre and labelled $\mathcal{R}_{8,13}$ (Table 3). The annulus dimensions were found by experimentation (using the profiles of field stars in the star-centred stack) to ensure that the flux within the annulus is dominated by the coma and sufficient to overcome the noise due to the sky background. In our stacked data, only 3 per cent of the flux of a point source is present in the wings of the PSF beyond an aperture of 8 pixel.

The R-band magnitude within the annulus $\mathcal{R}_{8,13}$ is $m_{8,13} = 20.95 \pm 0.03$ mag (see Table 4). The magnitude $m_{8,13}$ can be converted to a total dust cross-section, A_d, using equation (1) if we use the latter instead of the nucleus cross-section πr_e^2. In this case, p_R and β are the R-band albedo and linear phase coefficient of the dust particles, also unknown for P/LG. We assumed that these values are the same as for the nucleus ($\beta = 0.02$ mag deg^{-1} and $p_R = 0.1$) and found a total dust cross-section area $A_d \sim 2 \times 10^7$ m^2. This figure is uncertain by at least a factor of 2 mainly due to the uncertainty in the albedo.

Table 4. Photometry.

Region measured	B band (mag)	V band (mag)	R band (mag)
m_4	21.94 ± 0.05	21.42 ± 0.05	20.95 ± 0.03
$m_{4,8}$	22.31 ± 0.08	21.66 ± 0.08	21.21 ± 0.05
$m_{8,13}$	22.56 ± 0.16	21.80 ± 0.13	21.33 ± 0.08
$m_{13,20}$	22.72 ± 0.30	22.04 ± 0.27	21.47 ± 0.15

To convert the dust cross-section, A_d, to a dust mass, M_d, we assume that the dust consists of equal-sized spheres with an equivalent radius, r_d, representative of their true size distribution (e.g. Li et al. 2011). The mass is then given by

$$M_d = (4/3)\rho_d r_d A_d, \quad (3)$$

where ρ_d is the bulk density of the dust particles. We take an equivalent dust particle radius of $r_d = (0.1\ \mu\text{m} \times 1\ \text{cm})^{1/2} \approx 32\ \mu$m which is based on a power-law dust size distribution proportional to (dust grain radius)$^{-3.5}$ with minimum and maximum grain radii of 0.1 μm and 1 cm, respectively (Jewitt 2009; Li et al. 2011). We further assume a dust bulk density $\rho_d = 1000$ kg m^{-3} and find a total dust mass within the annulus $M_d \sim 8.6 \times 10^5$ kg.

The annulus crossing time, t_{cross}, is obtained by dividing the annulus projected width, $w_{cross} = 4 \times 10^6$ m (see Table 3), by the dust velocity, v_d. The velocity v_d is highly uncertain and depends on grain size (Crifo et al. 2004) but estimates based on macroscopic fragment ejection from 17P/Holmes (Stevenson, Kleyna & Jewitt 2010) and on the coma expansion velocities of 17P/Holmes (Montalto et al. 2008; Hsieh et al. 2010) and C/Hale-Bopp (Biver et al. 2002) vary from a few 100 to 1000 m s^{-1}. We take an intermediate $v_d = 500$ m s^{-1} and obtain an annulus crossing time

$$t_{cross} = \frac{w_{cross}}{v_d} \sim 0.8 \times 10^4\ \text{s}. \quad (4)$$

Finally, the mass-loss rate is given by $dM_d/dt = M_d/t_{cross} \sim 1.1 \times 10^2$ kg s^{-1}. At this rate, a nucleus of radius $r_e = 3$ km (see Section 4.1) and bulk density $\rho_{nuc} = 1000$ kg m^{-3} would have a sublimation lifetime $t_{sub} = 3 \times 10^4$ yr, significantly shorter than the dynamical lifetime of P/LG (see Section 5.2).

4.3 Nucleus and coma colour

We investigated the possibility that the nucleus and coma dust of P/LG have different colours by comparing the fluxes through different filters within the regions detailed in Table 3. To do so, we generated B- and V-band stacks as described in Section 4.1 using the frames with best image quality (6 × B band, seeing 1.0 × 1.1 arcsec^2; 6 × V band, seeing 0.8 × 0.9 arcsec^2) to obtain single

Table 3. Photometry regions.

Region label	Region shape	Aperture radius, r (pixel)	Aperture radius, ϕ (arcsec)	Projected radius, d (km)	Magnitudes in region	Dominant source
$\mathcal{R}_4$	Circle	4	0.96	3220	m_4	Nucleus (+ coma)
$\mathcal{R}_{4,8}$	Annulus	4–8	0.96–1.92	3220–6440	$m_{4,8}$	Nucleus + coma
$\mathcal{R}_{8,13}$	Annulus	8–13	1.92–3.12	6440–10 465	$m_{8,13}$	Coma
$\mathcal{R}_{13,20}$	Annulus	13–20	3.12–4.80	10 465–16 100	$m_{13,20}$	Coma

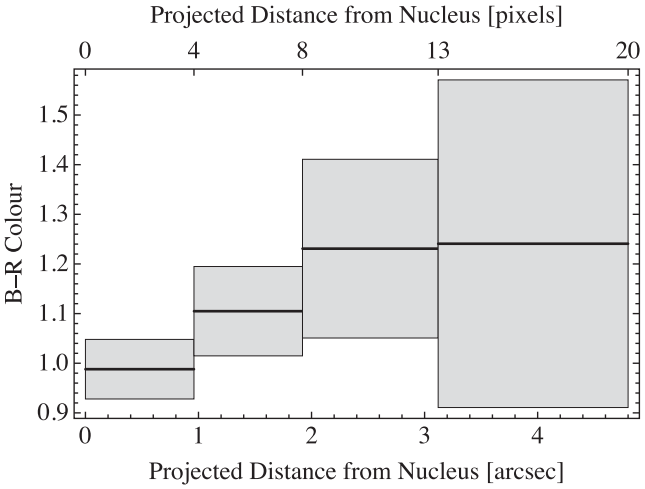

Figure 5. Radial variation of the $B - R$ colour (thick horizontal lines) and uncertainty (grey boxes). The average colours (thick horizontal lines) are shown in each of the four concentric regions described in Table 3. The coma-dominated annuli (apertures > 8 pixel) appear redder than the central region despite the large uncertainties.

images with equivalent exposure times of 1440 s in B (see Fig. 2) and 720 s in V. The resulting stacked images have $S/N_B \sim 32$ and $S/N_V \sim 34$ within the central aperture.

Fig. 5 plots the $B - R$ colour of P/LG versus projected distance from the nucleus, and Table 4 lists the B, V and R apparent magnitudes in the regions of interest. The comet nucleus region, $\mathcal{R}_4$, has colours $B - R = 0.99 \pm 0.06$ mag and $V - R = 0.47 \pm 0.06$ mag, typical of JFC nuclei (Jewitt 2002; Snodgrass, Lowry & Fitzsimmons 2006). Further from the nucleus, as the flux becomes dominated by the coma, the $B - R$ colour becomes slightly redder. Despite the large uncertainties the effect is noticeable and suggests that the coma dust may have a different colour from the nucleus.

4.4 Light curves

We searched for photometric variability in the P/LG data using the individual frames taken in B, V and R over the course of the night. Periodic photometric variations from the central region can signal a rotating, elongated nucleus, while temporal variations in the outer coma regions may indicate variable activity from the comet. To look for photometric variations, we performed photometry within the regions listed in Table 3 for each frame. As part of our observing strategy, we acquired sets of three consecutive images per filter. That allowed us to take the median magnitude of each set and divide the median uncertainty by $\sqrt{3}$.

Fig. 6 shows the resulting B, V and R light curves in regions $\mathcal{R}_4$, $\mathcal{R}_{4,8}$ and $\mathcal{R}_{8,13}$. Since we are only interested in the relative variability, the light curves for each band were median subtracted for alignment purposes. The light curves within each region were then shifted vertically for clarity of presentation.

The small variability seen in B and R within the central region $\mathcal{R}_4$ is probably not significant: the magnitudes m_4 in B and R display a positive correlation with atmospheric seeing, at a level that has a probability of only 4 per cent of occurring by chance. The large-scale variation observed in $m_{8,13}$, in all three bands, does not correlate with seeing or airmass and is probably real. Although the formal photometric uncertainties are large, the variation is regular. However, our time base is short rendering the interpretation difficult.

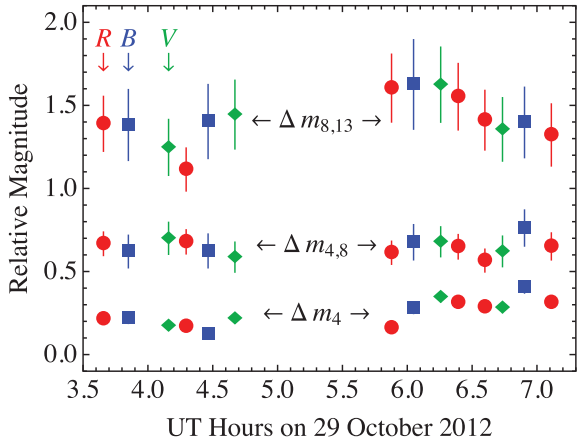

Figure 6. Light curves of comet P/LG sampling the central region $\mathcal{R}_4$ (Δm_4, measured within a 4 pixel or 0.96 arcsec radius aperture), the intermediate region $\mathcal{R}_{4,8}$ ($\Delta m_{4,8}$, from 0.96 to 1.92 arcsec) and the coma-dominated region $\mathcal{R}_{8,13}$ ($\Delta m_{8,13}$, from 1.92 to 3.12 arcsec). For each region, we plot relative magnitude light curves in bands B (blue squares), V (green diamonds) and R (red circles). The light curves in different bands were aligned simply by median subtraction, and the light curves in each region (Δm_4, $\Delta m_{4,8}$, $\Delta m_{8,13}$) were shifted vertically for clarity of presentation.

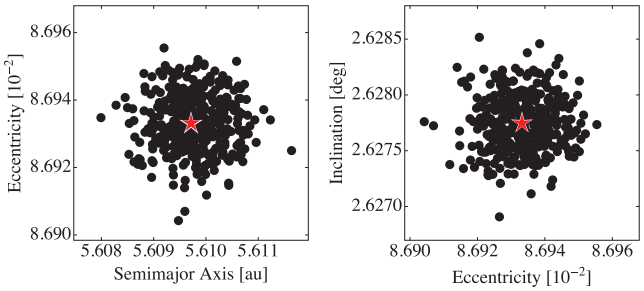

Figure 7. Initial orbital parameters of 370 clones of P/LG used in our numerical simulations. The clones are drawn from Gaussian distributions with centres on the actual orbital elements of P/LG (star symbol) and standard deviations equal to one-thousandth of the central value.

5 DYNAMICAL PAST AND FUTURE

Discovered by the LINEAR survey in 2010 October, P/LG was initially classified as a Jupiter Trojan. The object retained its Trojan status within the Jet Propulsion Laboratory (JPL) Horizons system until 2011 October, when cometary activity was detected (Grauer et al. 2011), at which point it was reclassified as a JFC. Currently, P/LG has a low inclination ($i = 2\overset{\circ}{.}6$), nearly circular orbit ($e = 0.09$) with a semimajor axis $a = 5.6$ au. The difference between the distances to perihelion and aphelion is a mere 1 au, leading to a surface temperature variation of $\Delta T = 15$ K (blackbody in equilibrium with sunlight). Such a temperature difference seems too small to cause periodic activity close to perihelion as is the case for most JFCs. This issue is discussed in more detail in Section 6.

To investigate the past and future dynamical evolution of P/LG, we numerically integrate its current orbit backwards and forwards in time. For this purpose, we use the N-body integration package MERCURY version 6.2 (Chambers 1999). We integrate the orbits of 371 objects, P/LG plus 370 clones with normally distributed orbital elements centred on P/LG's current orbit and with a 1σ dispersion equal to 10^{-4} of each parameter (Fig. 7). The Sun and eight major planets are included as massive bodies and the 371 P/LG clones as massless test particles. We use MERCURY's hybrid algorithm mode

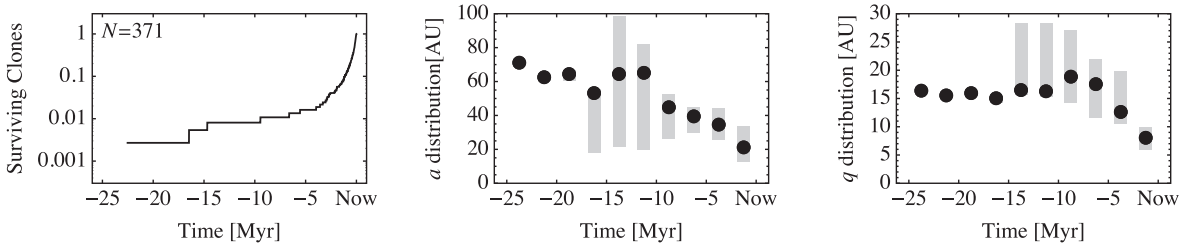

Figure 8. Past orbital evolution of the 371 clones of P/LG. The fraction of surviving clones (left) decreases steeply as their orbits are integrated back in time. Half of the clones do not survive the orbital integration beyond $t = -182$ kyr. The longest surviving clone reaches −22.5 Myr. The surviving clones evolve into Centaur/scattered KBO orbits with increasing median semimajor axis (black points in the centre plot) and median perihelion distance (black points in the right-hand plot). The grey boxes contain the central 50 per cent of the distribution in each time bin.

which combines a second-order mixed-variable symplectic algorithm with a Bulirsch–Stoer integrator to handle close encounters. We select an initial time step of 8 d and remove clones that go beyond 200 au from the Sun at any point during the dynamical evolution.

We note that our simulations of the orbital evolution of P/LG neglect non-gravitational forces. Collimated sublimation jets accelerate the nucleus and may alter the evolution presented here. An upper limit to this effect can be calculated assuming that the non-gravitational acceleration, T, is due to a single sublimation jet, always aligned tangentially along the orbit of the comet, through which all mass loss occurs. In that case, the rate of change of the semimajor axis, $\mathrm{d}a/\mathrm{d}t$, can be written as

$$\mathrm{d}a/\mathrm{d}t = 2Va^2T/(GM_\odot), \tag{5}$$

where V is the orbital velocity, G is the gravitational constant, $M_\odot$ is the mass of the Sun and the acceleration due to the jet is

$$T = (\mathrm{d}M_\mathrm{d}/\mathrm{d}t)(v_\mathrm{d}/m_\mathrm{nuc}). \tag{6}$$

Substituting $\mathrm{d}M_\mathrm{d}/\mathrm{d}t = 10^2$ kg, $v_\mathrm{d} = 500$ m s^{-1}, $m_\mathrm{nuc} = 1.1 \times 10^{14}$ kg and taking V as being the circular velocity at $a = 5.6$ au we obtain $\mathrm{d}a/\mathrm{d}t = 1.4 \times 10^{-5}$ au yr^{-1}. In the sublimation lifetime ($t_\mathrm{sub} = 3 \times 10^4$ yr) of comet P/LG its orbit can decay by $(\mathrm{d}a/\mathrm{d}t) \times t_\mathrm{sub} = 0.42$ au. This value is a strong upper limit, as it assumes a jet geometry contrived to achieve maximum orbital decay.

5.1 Orbit stability

Our simulations show that P/LG is dynamically unstable on very short time-scales. The 1σ spread of the main orbital parameters (semimajor axis, eccentricity, inclination) of the cloud of P/LG clone particles expands by a factor of e in only 12–14 yr into the past and about 100 yr into the future. These times provide a reasonable estimate of the Lyapunov time-scale for P/LG.

Due to the strongly chaotic nature of the orbit of P/LG, we can expect at best to obtain a statistical assessment of the past and future evolution of this comet. The chaotic evolution also implies that long-term integrations into the past or future are statistically equivalent (Levison & Duncan 1994; Horner, Evans & Bailey 2004). However, current close encounters between P/LG and Jupiter (see Section 5.3) generate an asymmetry in the dynamical evolution making it interesting to investigate the short-term past and future cases separately. Those same close encounters lead to further strong divergence of the clone orbits reinforcing the need for a more statistical analysis beyond a few kyr from the current time.

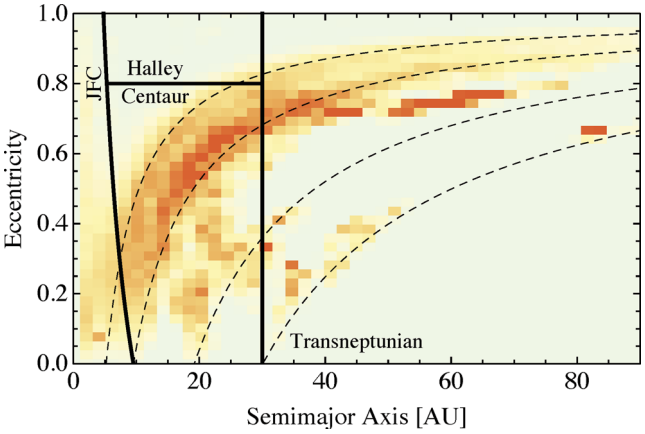

Figure 9. Heat map of the evolution of P/LG clones during the backwards integration described in Section 5. Darker patches have been occupied for a longer time by clones. The $a-e$ space is divided into four regions, representative of JFCs: $a < a_\mathrm{S}/(1+e)$, Centaurs: $a_\mathrm{S}/(1+e) < a < a_\mathrm{N}$ and $e < 0.8$, Halley comets: Centaurs with $e > 0.8$, and trans-Neptunian objects: $a > a_\mathrm{N}$, where a_S and a_N are the semimajor axes of Saturn and Neptune, respectively. Dashed lines mark the perihelia of Jupiter, Saturn, Uranus and Neptune. The clones spend most of the time as Centaurs, although pathways exist that transport clones to the trans-Neptunian region.

5.2 Orbit history

When integrating into the past we find that 50 per cent of the clones are removed from the simulation by $t = -182$ kyr. The longest lived clone reaches $t = -22.5$ Myr. The fraction of surviving clones is plotted versus time in Fig. 8 (left-hand panel). Each step in the figure corresponds to the removal of one clone, so e.g. only three clones survive to times earlier than $t = -10$ Myr. The figure also shows the median semimajor axis and perihelion distance of the surviving clones. The former increases with time into the past, albeit with large scatter (indicated by the grey boxes which contain the central 50 per cent of the points). The latter increases to about $q \sim 17$ au and then remains approximately constant with a tail towards larger q. The past evolution suggests that P/LG has recently evolved into its current orbit from a Centaur-type orbit.

Fig. 9 shows a heat map of the evolution of the P/LG clones in the semimajor axis versus eccentricity plane. Darker/redder regions are more often visited by clones as their orbits evolve backwards in time. The plane is divided into four regions, taken roughly to represent four types of orbits: *JFC-type*, defined as having $a < a_\mathrm{S}/(1+e)$, *Centaur-type*, bound by $a_\mathrm{S}/(1+e) < a < a_\mathrm{N}$ and $e < 0.8$, *Halley-type*, similar to Centaur-type except with $e > 0.8$, and *trans-Neptunian-type*, with $a > a_\mathrm{N}$, where a_S and a_N are the

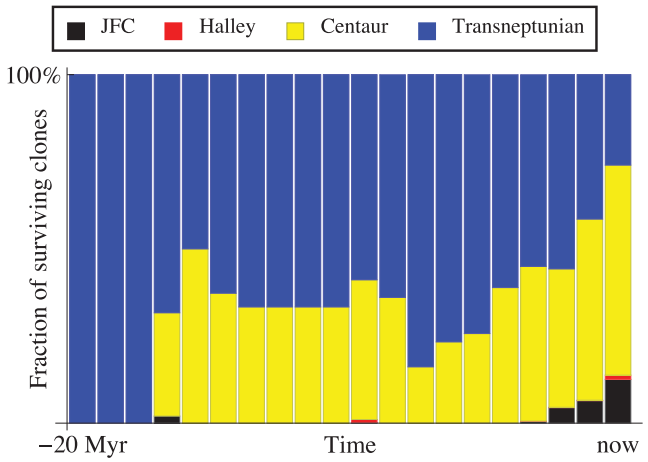

Figure 10. Fraction of surviving clones within each of the regions (orbit types) described in Fig. 9 plotted against time. Bins are 1 Myr wide. The leftmost three bins (−17 to −20 Myr) contain a single clone (see Fig. 8).

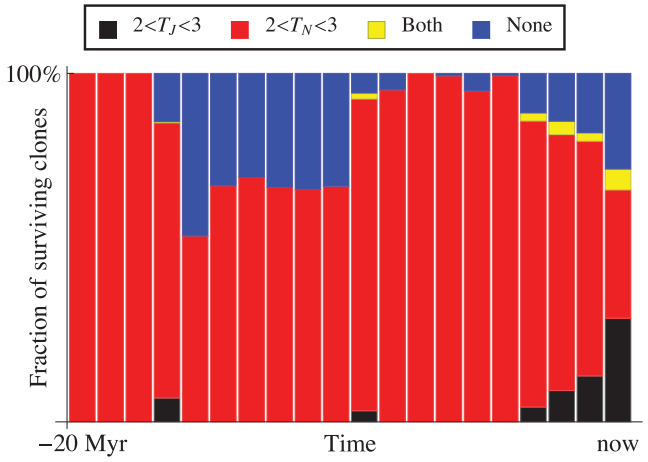

Figure 11. Evolution of the Tisserand parameter of clones. Myr-wide bins show the fractions of clones that have Tisserand parameter $2 < T \leq 3$ with respect to Jupiter, Neptune, both planets or none. A value of $2 < T \leq 3$ with respect to a given planet indicates that planet dominates the orbit of the object. The figure shows that, as time evolves into the past, Jupiter hands control to Neptune as the main influence to the clone orbits.

semimajor axes of Saturn and Neptune, respectively. These regions do not aim at accurately representing the dynamical behaviour of clone particles; they are designed simply as a means to classify the type of orbit occupied by the clones as a function of time. The figure shows that clones evolve mainly along constant-perihelion lines, as their semimajor axis and eccentricity increase. Fig. 10 traces the history of clones across the a–e plane as a function of time. The figure shows the fraction of surviving clones within each of the orbit-type regions described above in bins of 1 Myr, 20 Myr into the past. As already seen in Fig. 8, the surviving clones tend to quickly move away from the JFC region into Centaur-type orbits. Beyond just a few Myr into the past the semimajor axis of the surviving clones moves even further away from the Sun, into the trans-Neptunian region. The last surviving clone possesses a semimajor axis and eccentricity typical of a scattered trans-Neptunian object ($a \sim 80$ au, $e \sim 0.65$).

In Fig. 11, we show the history of the Tisserand parameter of P/LG clones with respect to Jupiter and Neptune in our numerical simulation. The Tisserand parameter is a useful dynamical quantity that is conserved in the restricted three-body problem. Here, the three bodies are the Sun, a planet and P/LG. In the Solar system, the Tisserand parameter is not exactly conserved, but when calculated for a given pair of small body and planet it can be used to quantify the dynamical influence the latter has on the former. For instance, the JFCs have Tisserand parameters $2 < T_{\rm J} < 3$ with respect to Jupiter, to which their orbits are strongly dynamically coupled. Main belt asteroids have $T_{\rm J} > 3$ and are relatively stable with respect to the Jovian gas giant. The Tisserand parameter of P/LG, calculated with respect to planet P, is given by

$$T_{\rm P} = a_{\rm P}/a + 2\sqrt{(1-e^2)(a/a_{\rm P})}\cos i, \qquad (7)$$

where $a_{\rm P}$ is the semimajor axis of the planet and a, e and i are the semimajor axis, eccentricity and inclination of P/LG, respectively. As shown in Fig. 11, within the first 1 Myr into the past the clones of P/LG are controlled partly by Jupiter ($2 < T_{\rm J} < 3$), partly by Neptune ($2 < T_{\rm N} < 3$) and partly by neither of those two planets. The latter indicates orbits between Jupiter and Neptune. Further into the past, Jupiter becomes less important dynamically while Neptune becomes more dominant.

In summary, our simulation results conspire to suggest that P/LG may be a recent arrival in the inner Solar system, possibly from a Centaur or trans-Neptunian-type orbit. That makes this object an interesting target of study as it may offer a glimpse of a relatively unprocessed Centaur.

5.3 Close encounters with Jupiter and the Trojan clouds

We performed a high time-resolution simulation (0.1 yr initial time step) going back only 3000 yr to investigate recent close encounters between the P/LG clones and the major planets. We focus here on Jupiter, due to its current close proximity to P/LG. In the very near past, we find that of the 371 P/LG clones, 331 (89 per cent) had close encounters with Jupiter (<100 planet radii) between 48 and 51 yr ago. During that time interval, 34 clone particles came within 20 Jupiter radii ($r_{\rm J}$) of the giant planet and the closest approach distance for any particle was $13r_{\rm J}$. Two of the 331 clone particles had very close approaches to Jupiter in consecutive orbits: one particle came within $14.0r_{\rm J}$ just 48 yr ago and within $8.7r_{\rm J}$ during the previous orbit (60 yr ago); another particle passed at $16.0r_{\rm J}$ and $14.6r_{\rm J}$ about 48 and 57 yr ago. Finally, if we consider the full 3000 yr time span of the simulation, seven particles came within the Roche limit of Jupiter ($\approx 2.7r_{\rm J}$ assuming a fluid-like P/LG nucleus with bulk density $\rho_{\rm nuc} = 1000$ kg m^{-3}; Asphaug & Benz 1996). In a similar integration to the one just described but into the future, we find that 11 out of the 371 clone particles come within $10r_{\rm J}$ and three of those come within $2r_{\rm J}$ roughly 145 yr into the future. A total of 41 clone particles approach Jupiter within $100r_{\rm J}$ at that time.

We also searched for possible crossings of one of the Jovian Trojan clouds by P/LG clones. The Trojan clouds have an irregular shape, roughly $4 \times 2 \times 0.5$ au (full width at half-maximum) in size (Jewitt, Trujillo & Luu 2000; Nakamura & Yoshida 2008). To identify potential crossings and estimate the time spent by clones inside the Trojan clouds, we used Jupiter's position to calculate the positions of its L3 and L4 Lagrangian points in each time step. Finally, for each clone we added the time steps it spent within 0.3 au of either L3 or L4. We chose 0.3 au to ensure that the clone is well within the densest region of the Trojan clouds. We found that clones spend an average of 10.1 of the last 3000 yr within the regions just described.

6 DISCUSSION

Fig. 4 shows P/LG as seen by the Pan-STARRS PS1 survey (see Section 2) close to the time the comet was discovered by LINEAR. The PS1 images show that P/LG was active at the time of discovery and yet the LINEAR pipeline first classified this object as a Jovian Trojan. This suggests that LINEAR may have misclassified several active objects as inert asteroids, which is an important point to consider at a time when the study of active asteroids is receiving increasing interest (Jewitt 2012 and references therein).

Our data reveal that P/LG was active in 2010 October, roughly 60° past perihelion, and remains active a year later, at 90° past perihelion. P/LG's nearly circular orbit, atypical for a JFC, leads us to consider a number of explanations for its activity. One possibility is that P/LG has been activated by a recent collision with a smaller object. We find this unlikely: our simulations show that P/LG spent only a negligible fraction of its recent past within the Trojan clouds (but see below), and even there the chance of a collision on to its $r_e < 3$ km nucleus would be low (intrinsic collision probability $P_i = 6.5 \times 10^{-18}$ km^{-2} yr^{-1}; dell'Oro et al. 1998). Another possibility is that P/LG was exposed to significant tidal stress due to close approaches to Jupiter. This scenario would require encounters with Jupiter closer than the Roche limit (mass shedding begins at $d < 0.69R_{\rm roche}$ for a comet on a parabolic orbit; Sridhar & Tremaine 1992; Asphaug & Benz 1996) which our simulations show to be improbable. It is also possible that P/LG became active due to rotational mass shedding but since the rotation period of P/LG is not known this possibility is untestable. One scenario that our simulations cannot rule out is that P/LG originated in the Trojan population and was dislodged from the 1:1 resonance with Jupiter through the action of non-gravitational effects (see Section 5). Conceivably, P/LG could have been collisionally activated by a smaller Trojan and led to drift from the stable region, accelerated by mass-loss jets; we note that P/LG's highly unstable orbit implies a recent departure from the Trojan region. Modelling this possibility is a complex task involving a number of unknown parameters and is beyond the scope of this paper but future observations of this comet may shed light on a possible link with the Trojan population.

The activity of P/LG could simply be due to ice sublimation. At first sight, the small difference between the P/LG perihelion and aphelion distances (Table 1), and the consequently small orbital variation of the subsolar equilibrium temperature ($\Delta T \approx 15$ K) could seem insufficient to power periodic sublimation activity. However, between the perihelion and aphelion distances of P/LG, the specific mass-loss rate due to water–ice sublimation varies by more than an order of magnitude (from 10^{-5} to 10^{-4} kg m^{-2} s^{-1}) while CO/CO$_2$ sublimation-driven mass loss varies by a factor of 2 and is around 10^{-2} kg m^{-2} s^{-1} (Jewitt 2009). We find that P/LG loses mass into the coma at a rate $\sim 10^2$ kg s^{-1} implying that an area of 10^6–10^7 m^2 would need to be active on the surface of P/LG if water–ice sublimation is the source of the activity. Those areas are small compared to the maximum surface area of the nucleus, $4\pi r_e^2 \sim 10^8$ m^2. Sublimation due to CO/CO$_2$ would require only an area $\sim 10^4$ m^2 to be active, corresponding to a tiny active vent on the surface of the 3-km nucleus. We conclude that given the recent perihelion passage and the particular range of heliocentric distances traversed by P/LG since then our estimated current mass-loss rate is consistent with the activity being driven by ice sublimation.

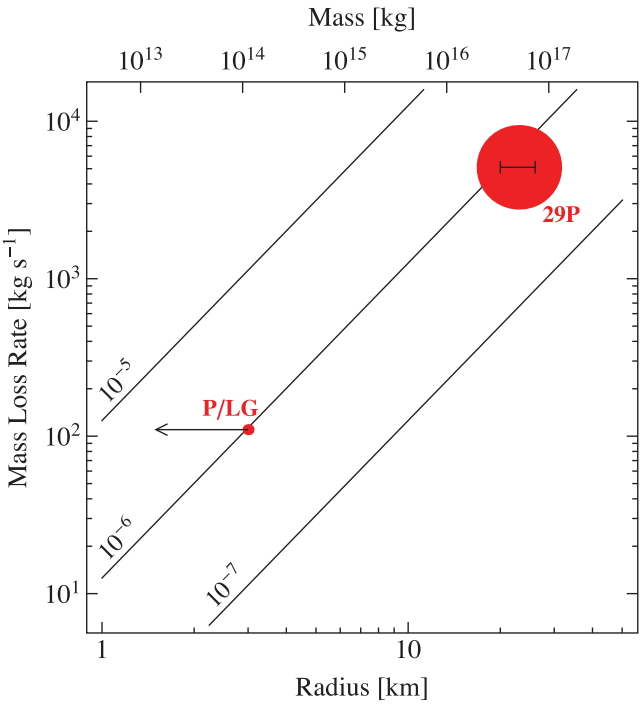

Figure 12. Comparison between comets P/LG and 29P. Mass-loss rates are plotted against nucleus radius (and mass, assuming nucleus/dust bulk density $\rho_{\rm nuc} = 1000$ kg m^{-3}). The arrow indicates that we possess only an upper limit on the nucleus radius of P/LG. The uncertainty in the radius of 29P is marked by a horizontal error bar. The size of the P/LG and 29P points is linearly proportional to their geometric cross-section for visual comparison. Lines of constant specific mass-loss rate are labelled in units of kg m^{-2} s^{-1}.

P/LG is in many ways comparable to comet 29P (see Table 5 and Fig. 12). Both comets have high perihelion ($q > 5$ au), low inclination ($i < 10°$), nearly circular orbits ($e < 0.1$) more typical of Centaurs than JFCs. Both orbits are unstable on very short timescales (a few hundred years; Horner et al. 2004). The two comets show similar levels of activity, with specific mass-loss rates close to $dm/dt = 10^{-6}$ kg m^{-2} s^{-1}, despite 29P being nearly an order of magnitude larger (>2 orders of magnitude more massive) than P/LG. Both objects display continued activity, although the coverage of P/LG reported here is not enough to establish a pattern of activity. It will be interesting to see if P/LG's activity is significantly

Table 5. Comparison between P/LG and 29P. Column 1: comet ID; column 2: semimajor axis; column 3: eccentricity; column 4: inclination; columns 5 and 6: broad-band colours; column 7: equivalent radius; column 8: model-dependent mass-loss rate; column 9: specific mass-loss rate. Mass assumes nucleus/dust bulk density $\rho_{\rm nuc} = 1000$ kg m^{-3}. Specific mass-loss rate assumes a spherical nucleus of radius r_e. Comet 29P colours from Jewitt (2009).

Comet	a (au)	e	i (°)	$B-R$ (mag)	$V-R$ (mag)	r_e (km)	M (kg)	dM/dt (kg s^{-1})	dm/dt (kg m^{-2} s^{-1})
P/LG	5.6	0.09	2.6	0.99 ± 0.06	0.47 ± 0.06	<3	1.1×10^{14}	1.1×10^2	7.7×10^{-7}
29P	6.0	0.04	9.4	1.28 ± 0.04	0.50 ± 0.03	23 ± 3	5.1×10^{16}	5.1×10^3	9.7×10^{-7}

modulated by its orbital motion or if it remains constant as is the case for comet 29P. It will also be of interest to monitor P/LG and see if it too will display the sporadic outbursts seen in 29P. Significant differences include the size of the comets and the source of activity: 29P is dominated by CO sublimation, while P/LG is more likely active due to water–ice sublimation.

7 CONCLUSIONS

We report photometric observations and numerical simulations of the orbital evolution of the unusual comet P/LG. Our findings can be summarized as follows.

(i) Comet P/LG was active at the time of discovery (2010 October) by LINEAR and remains active in 2011 October. LINEAR did not detect the activity and initially misclassified P/LG as a Trojan, which suggests that several active objects may have gone undetected by the survey.

(ii) The nucleus of P/LG has equivalent radius $r_e < 3$ km, and colours $B - R = 0.99 \pm 0.06$ mag and $V - R = 0.47 \pm 0.06$ mag, values typical of JFCs. The data suggest a slight reddening of the dust colour with distance from the nucleus but the uncertainties are large. We find no significant rotational photometric variability from the nucleus region.

(iii) We obtain a model-dependent estimate of the mass-loss rate from P/LG of $\sim$100 kg s^{-1}. We favour water–ice sublimation as the simplest and most likely cause for activity in comet P/LG.

(iv) Our numerical simulations show that the orbit of P/LG is unstable on very short time-scales and suggest that it may be a Centaur that recently arrived in the inner Solar system, although other possibilities exist involving non-gravitational effects.

(v) Comet P/LG is in a number of ways reminiscent of the well-known 29P/Schwassmann–Wachmann 1. 29P is a comet/active Centaur that shows sporadic outbursts superimposed on a background of constant activity. Comet P/LG is an order of magnitude smaller (three orders of magnitude less massive) than 29P and yet displays similar activity per unit area. Comets 29P and P/LG are interesting as possible examples of relatively unprocessed Centaurs.

ACKNOWLEDGMENTS

I thank the referee, Mario Melita, as well as David Jewitt and Ivo Labbé for their helpful comments on the manuscript. I am grateful to Larry Denneau and Ken Smith for helpful assistance with the PS1 survey data. I also acknowledge Colin Snodgrass for kindly supplying an IRAF fringe removal routine optimized for EFOSC2.

The PS1 Surveys have been made possible through contributions of the Institute for Astronomy, the University of Hawaii, the Pan-STARRS Project Office, the Max-Planck Society and its participating institutes, the Max Planck Institute for Astronomy, Heidelberg and the Max Planck Institute for Extraterrestrial Physics, Garching, The Johns Hopkins University, Durham University, the University of Edinburgh, Queen's University Belfast, the Harvard–Smithsonian Center for Astrophysics, and the Las Cumbres Observatory Global Telescope Network, Incorporated, the National Central University of Taiwan, and the National Aeronautics and Space Administration under Grant No. NNX08AR22G issued through the Planetary Science Division of the NASA Science Mission Directorate.

REFERENCES

Asphaug E., Benz W., 1996, Icarus, 121, 225
Biver N. et al., 2002, Earth Moon Planets, 90, 5
Buzzoni B. et al., 1984, Messenger, 38, 9
Chambers J. E., 1999, MNRAS, 304, 793
Crifo J. F., Fulle M., Kömle N. I., Szego K., 2004, in Festou M. C., Keller H. U., Weaver H. A., eds, Nucleus–Coma Structural Relationships: Lessons from Physical Models, Univ. Arizona Press, Tucson, p. 471
Crovisier J., Biver N., Bockelee-Morvan D., Colom P., Jorda L., Lellouch E., Paubert G., Despois D., 1995, Icarus, 115, 213
dell'Oro A., PAolicchi F., Marzari P., Dotto E., Vanzani V., 1998, A&A, 339, 272
Grauer A. D., Sostero G., Melville I., Kasprzyk A., Howes N., Guido E., Spahr T., Williams G. V., 2011, IAU Circ., 9235, 1
Horner J., Evans N. W., Bailey M. E., 2004, MNRAS, 354, 798
Hsieh H. H., Fitzsimmons A., Joshi Y., Christian D., Pollacco D. L., 2010, MNRAS, 407, 1784
Jewitt D., 1990, ApJ, 351, 277
Jewitt D. C., 2002, AJ, 123, 1039
Jewitt D., 2009, AJ, 137, 4296
Jewitt D., 2012, AJ, 143, 66
Jewitt D., Luu J., 1989, AJ, 97, 1766
Jewitt D. C., Luu J. X., 2001, AJ, 122, 2099
Jewitt D. C., Trujillo C. A., Luu J. X., 2000, AJ, 120, 1140
Kolokolova L., Hanner M. S., Levasseur-Regourd A.-C., Gustafson B. Å. S., 2004, in Festou M. C., Keller H. U., Weaver H. A., eds, Physical Properties of Cometary Dust from Light Scattering and Thermal Emission, Univ. Arizona Press, Tucson, p. 577
Lamy P., Toth I., 2009, Icarus, 201, 674
Landolt A. U., 1992, AJ, 104, 340
Levison H. F., Duncan M. J., 1994, Icarus, 108, 18
Li J., Jewitt D., Clover J. M., Jackson B. V., 2011, ApJ, 728, 31
Meech K. J., Jewitt D. C., 1987, A&A, 187, 585
Melita M. D., Licandro J., 2012, A&A, 539, A144
Millis R. L., Ahearn M. F., Thompson D. T., 1982, AJ, 87, 1310
Montalto M., Riffeser A., Hopp U., Wilke S., Carraro G., 2008, A&A, 479, L45
Moroz L. V., Arnold G., Korochantsev A. V., Wasch R., 1998, Icarus, 134, 253
Nakamura T., Yoshida F., 2008, PASJ, 60, 293
Peixinho N., Doressoundiram A., Delsanti A., Boehnhardt H., Barucci M. A., Belskaya I., 2003, A&A, 410, L29
Peixinho N., Delsanti A., Guilbert-Lepoutre A., Gafeira R., Lacerda P., 2012, The bimodal colors of Centaurs and small Kuiper belt objects, A&A, 546, A86
Roemer E., 1958, PASP, 70, 272
Russell H. N., 1916, ApJ, 43, 173
Senay M. C., Jewitt D., 1994, Nat, 371, 229
Snodgrass C., Lowry S. C., Fitzsimmons A., 2006, MNRAS, 373, 1590
Snodgrass C., Saviane I., Monaco L., Sinclaire P., 2008, Messenger, 132, 18
Solontoi M. et al., 2012, Icarus, 218, 571
Sridhar S., Tremaine S., 1992, Icarus, 95, 86
Stevenson R., Kleyna J., Jewitt D., 2010, AJ, 139, 2230
Thompson W. R., Murray B. G. J. P. T., Khare B. N., Sagan C., 1987, J. Geophys. Res., 92, 14933
Tonry J. L. et al., 2012, ApJ, 750, 99
Trigo-Rodríguez J. M., García-Melendo E., Davidsson B. J. R., Sánchez A., Rodríguez D., Lacruz J., de Los Reyes J. A., Pastor S., 2008, A&A, 485, 599

This paper has been typeset from a TEX/LATEX file prepared by the author.